ADVANCED NANOBIOMED RESEARCH Open Access
www.advnanobiomedres.com

Functionalized Gold Nanoclusters Promote Stress Response in COS-7 Cells

Denver P. Linklater, Xavier Le Guével, Erim Kosyer, Sergey Rubanov, Gary Bryant, Eric Hanssen, Vladimir A. Baulin, Eva Pereiro, Palalle G.Tharushi Perera, Jason V. Wandiyanto, Ana Angulo, Saulius Juodkazis, and Elena P. Ivanova**

Ultrasmall gold nanoclusters (AuNC) show great promise for application in theranostics due to their unique optical and physicochemical properties; however, the associated nanotoxicology concerns need to be carefully considered because of their high diffusion across the cellular barrier. Herein, new insights into the role of surface modification of 2 nm AuNC on their toxicity with impact on the metabolism of COS-7 fibroblast-like cells are revealed. AuNCs are chemically modified with either a monodentate-thiolated molecule (AuNC-MHA) or a modified-bidentate sulfobetaine zwitterionic molecule (AuNC-ZwBuEt). Uptake and localization inside fibroblasts and the resultant influence on cell ultrastructure are carefully evaluated using scanning transmission electron microscopy (STEM) and cryo-soft-X-ray tomography (cryo-SXT). At concentrations of ≥25 μg Au mL^{-1}, AuNC-ZwBuEt are cytotoxic toward COS-7 cells and are observed to cross the nuclear membrane. Cryo-SXT analysis shows that fibroblasts develop an acute stress response in the form of swollen mitochondria, nuclear membrane blebbing, and large cytoplasmic vacuoles as early as 1 h postexposure. By contrast, AuNC-MHA are not cytotoxic toward COS-7 cells. Endosomal escape and translocation of the AuNC-ZwBuEt into the nucleus and other organelles may be the cause for the observed cytotoxicity and highlight the need for further study of metal nanocluster-cell interactions.

1. Introduction

Gold nanoclusters (AuNCs), consisting of an assembly of a defined number of atoms (typically between tens and hundreds), exhibit distinct electronic states enabling tunable photoluminescence from ultraviolet (UV) to near-infrared (NIR/SWIR) wavelengths. As such, AuNCs may be useful for in vitro cell labeling and in vivo imaging applications.[1–7] For example, AuNCs (<3 nm core diameter), protected by thiolate ligands, have recently been demonstrated to enable excellent computed tomography imaging of tumors.[8–11] AuNCs can be tracked in real time in various organs, making them an important theranostic tool.[12,13] Their subnanometer size strongly impacts their interaction with biological components (i.e., protein corona[14]) and with biological barriers at the tissue and cellular levels (high diffusivity).[3,8,15] Furthermore, the rapid tissue diffusion of AuNCs is enabled by their small size and permeability, allowing accumulation in the tumor microenvironment

D. P. Linklater, E. Kosyer, G. Bryant, P. G. T. Perera, E. P. Ivanova
STEM College
School of Science
RMIT University
Melbourne, VIC 3000, Australia
E-mail: denver.linklater@rmit.edu.au; elena.ivanova@rmit.edu.au

X. Le Guével
Cancer Targets and Experimental Therapeutics
Institute for Advanced Biosciences
University of Grenoble Alpes
38700 La Tronche, France

The ORCID identification number(s) for the author(s) of this article can be found under https://doi.org/10.1002/anbr.202200102.

DOI: 10.1002/anbr.202200102

S. Rubanov, E. Hanssen
Ian Holmes Imaging Centre
Bio21
University of Melbourne
Parkville 3052, VIC, Australia

V. A. Baulin
Departament de Química Física i Inorgànica
Universitat Rovira i Virgili
C/Marcel.lí Domingo s/n, 43007 Tarragona, Spain

E. Pereiro
MISTRAL Beamline-Experiments Division
ALBA Synchrotron Light Source
Cerdanyola del Vallès, 08290 Barcelona, Spain

J. V. Wandiyanto, S. Juodkazis
Optical Sciences Centre
Swinburne University of Technology
Hawthorn, VIC 3122, Australia

and leading to efficient renal elimination.[16] In vivo experiments show that Au nanoparticles (AuNPs) in the range of 5–200 nm are captured by the reticuloendothelial system (RES) for hepatic excretion.[17] By contrast, AuNCs with size below the kidney filtration threshold (KFT, ≈5.5 nm) are cleared rapidly via the kidneys.[18] Nevertheless, the toxicity of residual AuNC may still pose a problem when they are engineered for therapeutic and diagnostic use.[19] For instance, researchers reported a release of AuNC in blood circulation, being first sequestered in muscle tissue, indicating the importance of studying the long-term toxicity of such ultrasmall particles.[20]

In solution, AuNCs must be electronically stabilized by a surface ligand.[21] Functionalization of the AuNC surface allows application flexibility as they can exert their action at different specific sites. However, in turn, the nano–bio interactions of AuNCs can be significantly affected by their surface chemistry, leading to a poor understanding of their structure–function relationship in vitro. At the cellular level, AuNC size, surface chemistry, and hydrophobicity strongly influence particle interactions with biological membranes and affect particle uptake.[22–25] For example, AuNCs of 1.4 nm capped with triphenylphosphine monosulfonate (TPPMS) have been reported to provoke adverse reactions in eukaryotic cells, inducing necrosis, mitochondrial damage, and oxidative stress.[26] AuNPs with the same surface functionalization but a diameter of 15 nm did not induce the same devastating response in the cell lines as ultrasmall AuNCs, suggesting that the cytotoxicity of AuNCs might be size dependent.[26–28] Similarly, smaller (13 nm) gold nanoparticles were demonstrated to be more cytotoxic toward human kidney cells than larger (60 nm) nanoparticles.[29] AuNPs, along with silver (Ag) and platinum (Pt) nanoparticles, are known to cause renal toxicity.[30] Nanoparticles manifest renal toxicity through a combination of cell membrane damage, oxidative stress, mitochondrial injury, cytoskeletal changes, apoptosis, and necrosis;[30] however, the differences in the mechanisms of NP cytotoxicity (dependent on particle size and surface chemistry) toward different cell types have not been addressed.

While AuNCs modified for fluorescence in the NIR and SWIR regions for in vivo tumor imaging exhibit high renal clearance and elimination from multiple organs,[10,31] nevertheless, the fate of residual AuNC in the biological system, particularly in the kidneys, due to their role in the elimination of AuNC, at the cellular level is not clear. Indeed, the extent of fibrosis or tubulointerstitial damage within the kidneys is a key indicator of the prognosis for renal failure.[32] Thus, we aimed to study the cytotoxicity of AuNC toward African green monkey kidney-derived COS-7 fibroblast-like cells. We also aimed to clarify the effect of the AuNC functionalities on their biodistribution and cytotoxicity. In the current work, we investigated the fate of 2 nm AuNC modified with either a monodentate-thiolated molecule or a modified-bidentate sulfobetaine zwitterionic molecule to control cell membrane interactions in COS-7 fibroblasts using a combination of scanning transmission electron microscopy–energy-dispersive X-ray spectrometer (STEM–EDS) and cryo-soft X-ray tomography (cryo-SXT).

A. Angulo
Immunology Unit
Department of Biomedical Sciences
Faculty of Medicine and Health Sciences
University of Barcelona, Institut d'Investigacions Biomèdiques August Pi i Sunyer
Barcelona, Spain

2. Results

AuNCs of 2 nm diameter were synthesized according to a previously optimized protocol[33] and functionalized with a moderately hydrophobic monodentate-thiolated molecule, mercaptohexanoic acid (MHA), containing a short aliphatic chain with a terminal carboxyl group[34–36] and a more hydrophilic modified-bidentate sulfobetaine zwitterionic molecule (ZwBuEt).[23] Their respective surface characteristics are shown in **Table 1**. AuNC-MHA and AuNC-ZwBuEt have demonstrated good colloidal stability in water, buffer solution, and serum-containing medium for ≈6 months.[12,23,37,38]

2.1. AuNC Cytotoxicity toward COS-7 Cells

To assess the corresponding cytotoxicity of AuNC in COS-7 fibroblastic cells, we performed cell proliferation (MTS) assays following acute exposure (after 24 h) and 4 and 7 days postexposure to AuNCs functionalized with either MHA or ZwBuEt ligands to investigate cell recovery (or chronic impact) (**Figure 1**).[40] Cell viability and metabolic activity were assessed compared to the untreated (no AuNC exposure) sample by quantification of the reduction of tetrazolium salt compound by viable cells to a colored formazan dye. The color change is relative to the number of living cells and corresponds to the metabolic activity of the cells. At 24 h after exposure, at 25 $\mu g\,mL^{-1}$, AuNC-MHA showed no detrimental effect on cell viability as determined by no decline in the percentage of cell metabolic activity compared to the untreated cells. However, at higher concentrations (>50 $\mu g\,mL^{-1}$), AuNC-MHA influenced COS-7 metabolism after a 1 day exposure. There was a (nonsignificant) 30% reduction in cell metabolic activity at concentrations of 50 and 100 $\mu g\,mL^{-1}$ in comparison to the untreated control cells. Those cells exposed to 200 $\mu g\,mL^{-1}$ experienced increased cell metabolic activity; increased cell metabolic activity upon nanoparticle exposure has been associated with abnormal mitochondrial function.[41] However, this trend was not corroborated at day 4 postexposure

Table 1. Surface characterization of AuNC.

AuNC	Ligand structure	Size[a)][39]	Zeta potential (ζ)[b)][23]	Surface ligand logP
MHA	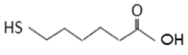	Width = 0.73 nm, length = 2.27 nm	−21.3 ± 0.5 mV	1.43
ZwBuEt	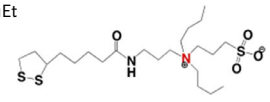	Width = 0.79 nm, length = 2.32 nm	−10.0 ± 0.2 mV	−3.45

[a)]As determined by SAXS measurements and includes Au core + ligand; [b)]At pH 7 in H_2O.

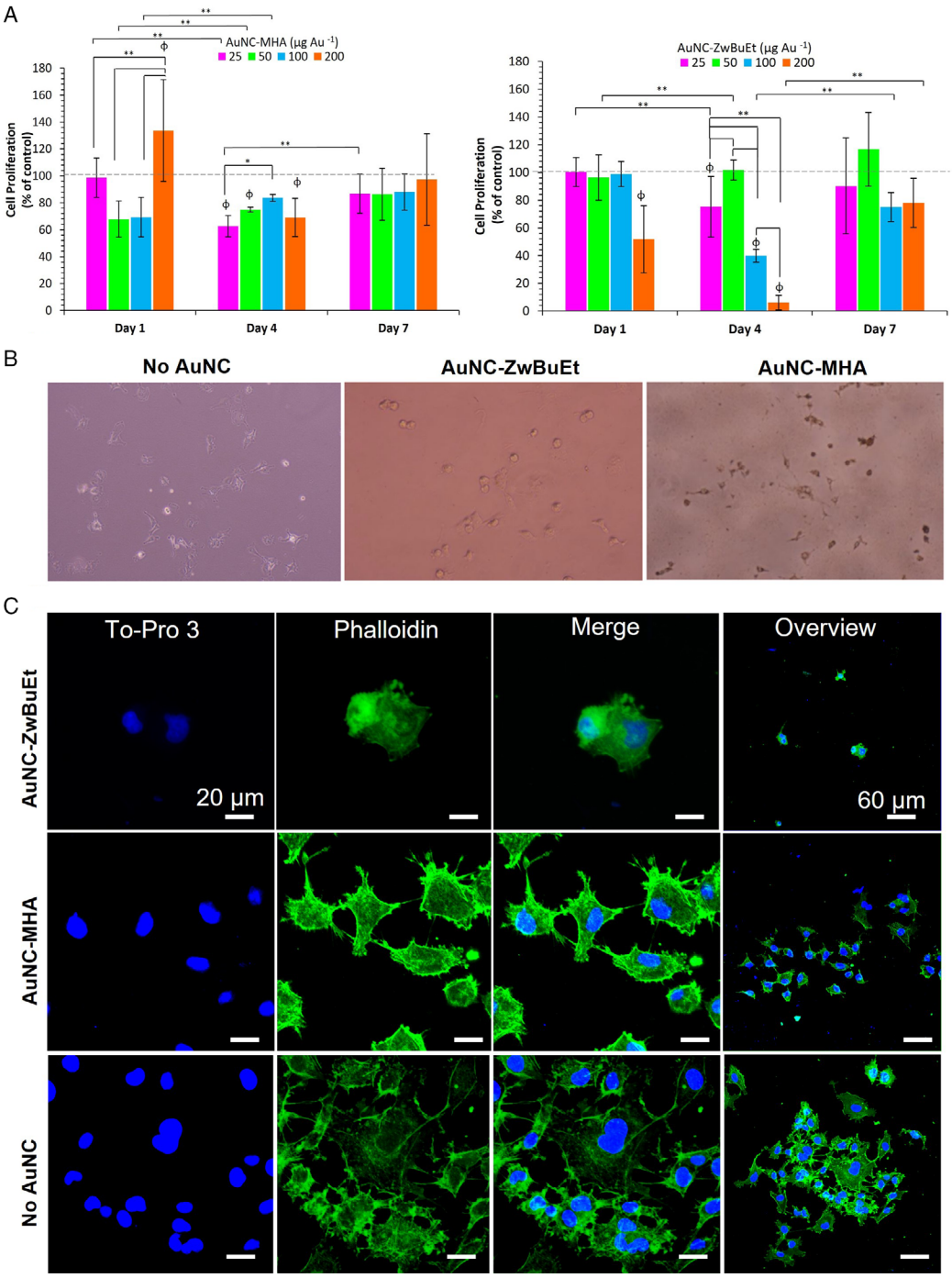

Figure 1. Viability of COS-7 fibroblasts incubated with AuNCs for 24 h and 4 and 7 days postexposure. A) Evaluation of the cell metabolic activity in the presence of AuNC-MHA and AuNC-ZwBuEt at concentrations of 25, 50, 100, to 200 μg Au mL^{-1} by MTS assay as a percentage of the control. Data are presented as the mean ± standard error ($n = 3$). Statistical significance is denoted by $^{**}p < 0.01$ and $^{*}p < 0.05$. ϕ denotes statistically significant values compared to the control ($p < 0.01$). *P*-values are calculated using one-way ANOVA with Tukey's post hoc test. B) Optical micrographs of COS-7 fibroblasts in culture post 24 h exposure to 100 μg Au mL^{-1} AuNCs. The color difference between the respective photographs can be attributed to adding AuNCs to cell media. COS-7 fibroblasts incubated with AuNC-MHA appear to be coated with particles. C) CLSM micrographs of the morphology of COS-7 fibroblasts 24 h exposure to 100 μg Au mL^{-1} AuNCs. The nucleus is stained with To-Pro 3 (blue); the actin network is stained with Phalloidin (green).

and cells exhibited decreased proliferation (approximate reduction of 30% in comparison to the control ($p < 0.01$)). Nevertheless, by day 7, COS-7 cells had recovered from AuNC-MHA exposure, and there were no statistically significant differences in cell metabolic activity between treated and non-treated samples (Figure 1A).

By contrast to AuNC-MHA, AuNC-ZwBuEt at the maximum concentration of 200 μg Au mL^{-1} induced a statistically significant reduction in cell metabolic activity of ≈50% ($p < 0.05$) after 24 h of exposure, whereas lower concentrations failed to impact cell metabolism negatively. However, by day 4, those cells treated with ≥100 μg Au mL^{-1} showed substantial reductions in cell proliferative activity of 60%. By day 7, there was an improvement in cell culture conditions; however, cell metabolism remained below that of the untreated sample (although the difference was not statistically significant), indicating that the reduced metabolism of MTS by COS-7 cells exposed to AuNC-ZwBuEt was a result of AuNC toxicity.

Actin staining was used to reveal the morphological changes to the cell cytoskeleton induced by AuNC exposure at concentrations of ≥100 μg Au mL^{-1} for 24 h and following recovery for 4 days. Fluorescence micrographs confirm that 24 h exposure to concentrations of 100 μg Au mL^{-1} AuNC-MHA does not adversely affect the cytoskeletal network of COS-7 fibroblasts. Confocal laser scanning microscopy (CLSM) micrographs show normal cellular morphology and cell spreading (Figure 1B,C). However, those cells exposed to AuNC-ZwBuEt exhibit a highly rounded morphology at day 1 with a disorganized actin network and more radial actin fibers than polarized actin fibers (Figure 1B,C). Previously, the uptake of 40 nm AuNPs has been associated with the cytoskeletal remodeling of endothelial cells.[42] By day 4, those cells treated with AuNC-MHA exhibited normal cell spreading and migration, indicating recovery from AuNC exposure (Figure S1, Supporting Information). Nevertheless, at day 4, AuNC-ZwBuEt-treated cells' proliferation rate is stunted, as confirmed by the MTS assay and that the cell number did not increase substantially from day 1 to day 4. Indeed, at higher concentrations (200 μg Au mL^{-1}), CLSM micrographs show that COS-7 cells failed to form cell surface extensions compared to untreated cells (Figure S2, Supporting Information). It has been hypothesized that cell apoptosis following AuNCs exposure results from the number of vacuoles in the cells, which may disrupt the cytoskeleton, causing cell area contraction and decreased motility.[43]

2.2. Surface-Ligand-Dependent Uptake of AuNC

Transmission electron microscopy (TEM) and STEM–EDS analysis of COS-7 fibroblasts exposed to AuNCs was used to confirm the presence of AuNC in cells and to identify changes to the cell ultrastructure (**Figure 2**). The TEM analyses clearly show that for AuNC-ZwBuEt, the particles are mostly sequestered inside large vesicles (lysosomal vacuoles [LV])[44] at both days 1 and 4 postexposure (Figure 2B) and rarely found free

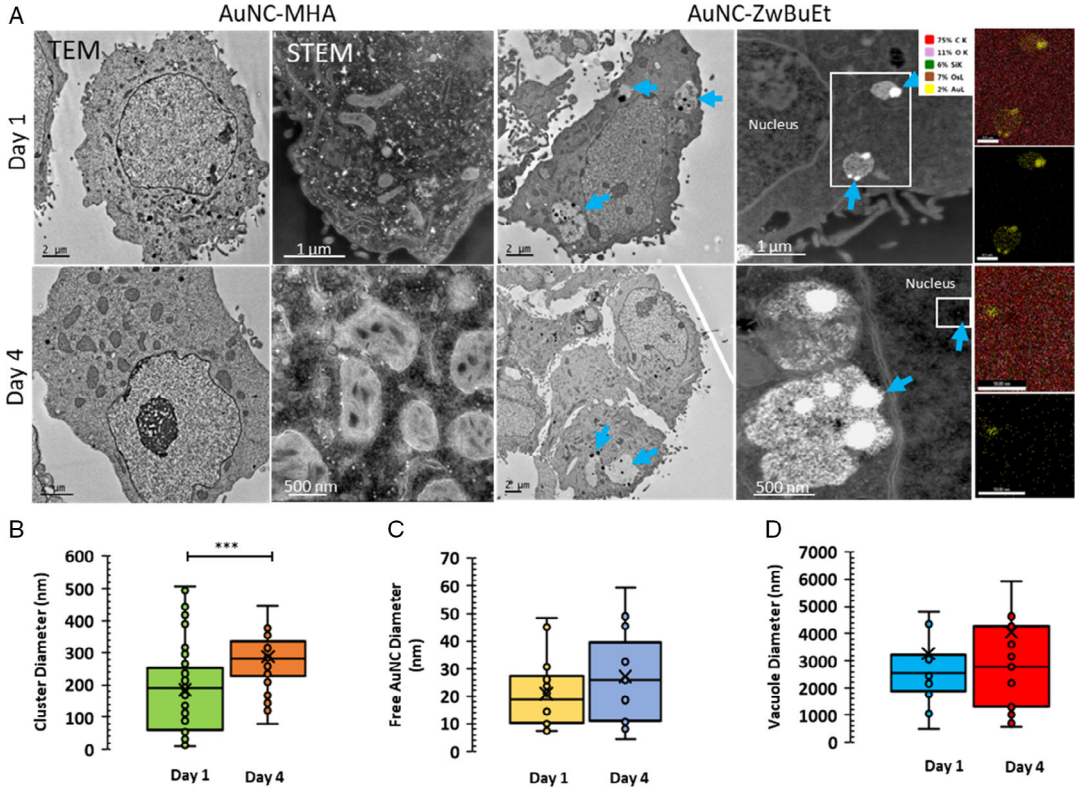

Figure 2. A) TEM and STEM micrographs of COS-7 fibroblasts 1 and 4 days postexposure to 100 μg Au mL^{-1}. Blue arrows indicate the presence of clusters of AuNCs in vesicles and within the cell nucleus. The presence of AuNC was confirmed by STEM/EDS elemental maps (right panels). Quantification of B) AuNC-ZwBuEt aggregate diameter localized inside vesicles, C) AuNC-ZwBuEt diameter localized within the cell cytoplasm and D) vacuole diameter. Data were determined from examination of 50 images. Vacuoles were measured on the long axis. Statistical significance is denoted by ***$p < 0.0005$, $n = 50$. *P*-values are determined using one-way ANOVA. At 1 and 4 days post-AuNC exposure, no AuNC-MHA were found localized within the cell cytoplasm or sequestered in vesicles.

within the cytoplasm. No AuNC-MHA were observable within the cells at any studied time points. In AuNC-ZwBuEt-treated cells, the vacuoles are distributed uniformly across the cytoplasm. We measured the size of the vesicles containing AuNCs and AuNC aggregates, as well as the size and density of the clusters within each LV. Aggregates of AuNC-ZwBuEt have a broad size distribution of 10–500 nm (with an average of 185 ± 132 nm) on day 1; this distribution was reduced by day 4 with AuNC-ZwBuEt aggregates possessing an average diameter of 287 ± 107 nm. There was no difference in the size of the vesicles on days 1 and 4 (Figure 2C). The larger AuNC aggregate sizes, in combination with the similarity in size of the LV, indicate that there is an accumulation of AuNC within the vesicles and that cells cannot efficiently transport the AuNCs out of the cell, even after 4 days post-AuNC exposure. STEM–EDS confirmed that the contents of the LVs were mainly free AuNC and aggregates of AuNC (Figure 2A).

Similarly, there was no difference in the diameter of free AuNC that were detected by microscopy within the cytoplasm. The morphology of untreated COS-7 fibroblasts is shown in Figure S3, Supporting Information. Close examination of STEM images also revealed that after 4 days, particles were detected inside the nucleus, as confirmed by STEM–EDS. By contrast, AuNC-MHA were not observed inside the cells through TEM or STEM–EDS analysis. In addition, cell vacuolization and numerous endocytic vesicles were not identified within the cell cytoplasm for those cells exposed to AuNC-MHA, as was observed for those exposed to AuNC-ZwBuEt.

2.3. Cryo-SXT Investigation of the Morphology of COS-7 Fibroblast Ultrastructure Following AuNC Uptake

Cryo-SXT experiments to assess the resultant morphology and changes in ultrastructure to COS-7 cells were conducted with the cells grown adherently on Quantifoil gold grids exposed to 100 μg Au mL^{-1} AuNC for 1 h (**Figure 3**). The 1 h incubation point was used to capture the initial interactions between the AuNC and cells and to pinpoint initial changes in cell ultrastructure in response to AuNC uptake compared to control COS-7 fibroblasts (Figure S5, Supporting Information). Figure 3B displays selected slices of tomographic reconstructions together with the segmented volume of the fibroblast, highlighting the localization of AuNC aggregates in representative cells. The reconstruction and segmentation of tomograms permitted analysis of the amount and location of internalized AuNC aggregates. After exposure to AuNC-MHA for 1 h, COS-7 fibroblast cell ultrastructure appears morphologically normal, although there is an increase in the number of endosomes present within the cytosol (of size 990 ± 186 nm).[45] Multiple endosomes are present in the cell cytoplasm that all possess AuNC aggregates with an average size of 31.5 ± 5.0 nm.

Furthermore, autophagic vesicles were identified as ones containing membrane-bound vesicles.[46] This result contrasts with the TEM and STEM analyses above that identified no AuNC-MHA localized within the cell cytoplasm or sequestered in vesicles. At 1 h, AuNC-MHA is confined chiefly to different intracellular compartments, such as endosomes and autophagosomes, limiting their interaction with ribosomes and mitochondria in the cytosol.[47] These compartments are crucial for eliminating NPs via extracellular vesicles from the cell cytoplasm,[47] suggesting that AuNC-MHA aggregates are efficiently transported out of the cell without causing significant deleterious effects.

By contrast, after exposure to 100 μg Au mL^{-1} AuNC-ZwBuEt for 1 h, COS-7 cells showed an extreme stress response. Large numbers of vacuoles can be observed in the cytoplasm, and the mitochondria appear severely swollen and enlarged (**Figure 4**). Mitochondrial morphology is directly related to cellular health. Segmentation allowed for the evaluation of the volume and shape of these organelles to obtain statistical information about morphological changes to the mitochondria after exposure to either AuNC-ZwBuEt or AuNC-MHA. The mitochondrial volume of AuNC-ZwBuEt-treated cells in Figure 4D demonstrates a significant increase in the size of mitochondria ($p < 0.01$). Previous research has shown that AuNCs exert detectable adverse effects on mitochondria. For example, human astrocytes treated with 10 μM glutathione-functionalized AuNC (AuNC-SG) of different core sizes increased the number of elongated mitochondria suggesting a rebalancing of mitochondrial fusion and fission.[48] In another example, cationic 5 nm AuNPs induced the formation of large vacuoles in the cytoplasm and caused the mitochondria to swell due to defective mitochondrial fission.[49] These observations are corroborated in the current work, where swollen mitochondria are indicative of cellular stress (particularly oxidative stress)[50] and mitochondrial dysfunction.[45,48,51] Cell vacuolization after NP treatment has been linked to the cell opening transmembrane water channels that allow an influx of external water.[52]

Additionally, autophagic compartments, or multivesicle bodies (MVBs), containing AuNC aggregates are observed in large numbers (Figure 4B), indicating the trigger of cell autophagy.[53] The nuclear membrane also shows signs of blebbing, which may be related to the beginning of cell apoptosis[54] (Figure 3, 4). AuNC-ZwBuEt aggregates were also free within the cytoplasm (Figure 4B), either due to passive translocation across the cell membrane or due to endosomal escape.[55]

3. Discussion

The current study demonstrated the importance of surface chemistry for the cytotoxicity of AuNCs toward fibroblastic cells. While moderately hydrophobic MHA-modified AuNCs were relatively noncytotoxic toward COS-7 cells, hydrophilic zwitterionic AuNC elicited pronounced cytotoxicity in the fibroblasts. Indeed, the interactions at the cell–AuNC interface seem to be highly influenced by the type of ligand coating the particles. The cellular uptake of nanoparticles is the first step toward inducing a cytotoxic response in mammalian cells and is influenced by initial nanoparticle–membrane interactions, which are further governed by surface chemistry.[56,57] Our results showed that the AuNC-MHA triggered autophagy, evidenced by cryo-SXT revealing the presence of autophagic vesicles in the cell cytoplasm at 1 h post-AuNC exposure. However, although endocytosis was not explicitly shown, AuNC-MHA were not evident within the cell cytoplasm or colocalized in endo/lysosomes at 24 h or 4 days post-AuNC exposure. By contrast, the autophagic

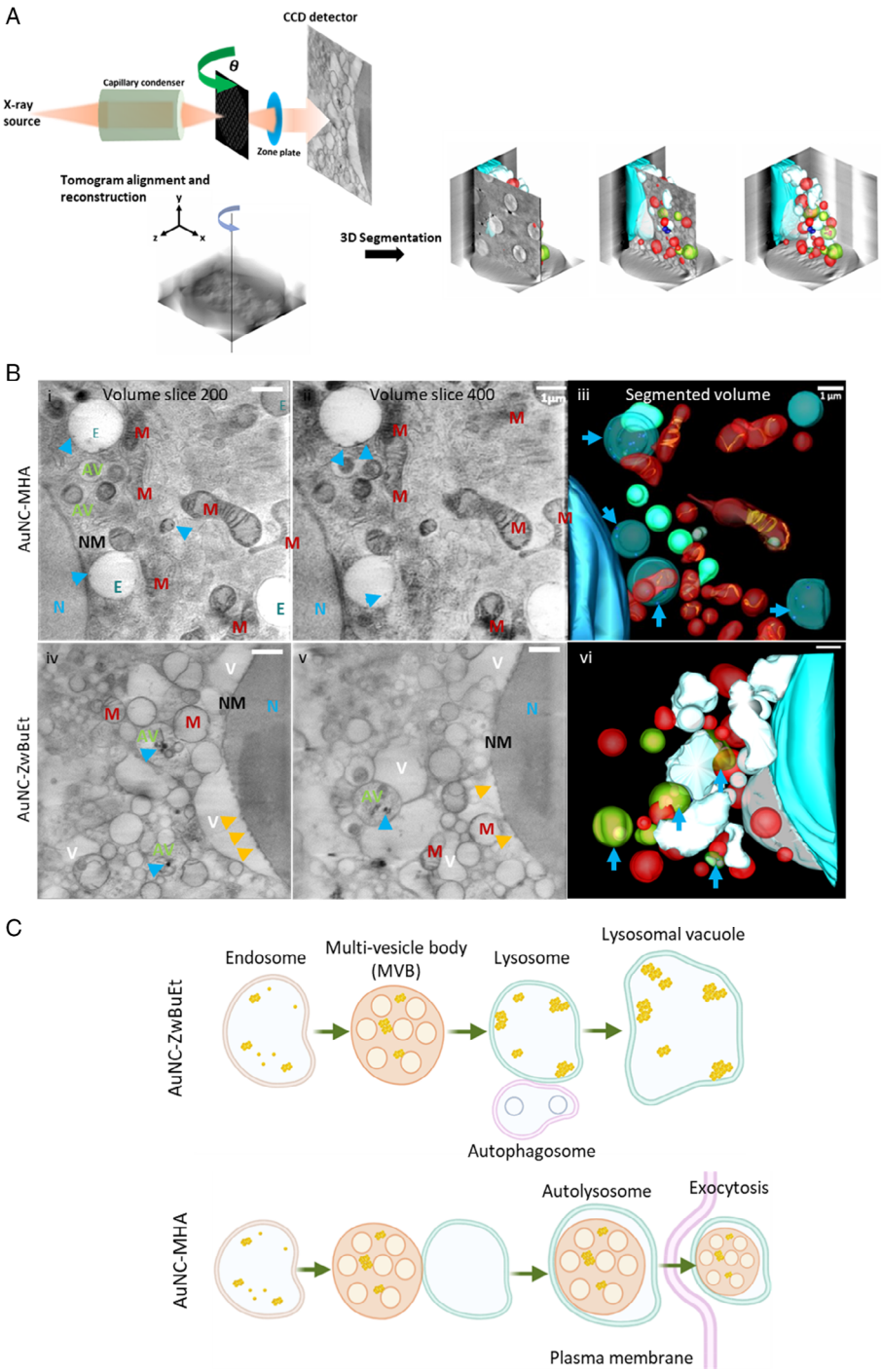

Figure 3. A) Schematic representation of the cryo-SXT setup at the Mistral beamline, ALBA. B) Selected slices of cryo-SXT tomograms and segmentation highlighting the effect of AuNCs on COS-7 fibroblast ultrastructure. Cells were exposed to 100 µg Au mL^{-1} for 1 h prior to vitrification. Cyan arrows indicate the presence of AuNCs in aggregates, and orange arrows indicate examples of cell damage. Those cells exposed to AuNC-ZwBuEt experienced significant changes to cell ultrastructure, including a higher number of intracellular vacuoles and blebbing of the nuclear membrane (orange arrows). M, mitochondria; E, endosome; AV, autophagic vesicle; L, liposome; NM, nuclear membrane; N, nucleus; V, vacuole. (C) Schematic of the proposed aggregation pathway of AuNC-ZwBuEt versus AuNC-MHA in COS-7 fibroblasts. Zwitterionic AuNCs form clusters in endosomes and multivesicle bodies before coalescing into larger aggregates in lysosomes. Autophagosomes merge with lysosomes to form autolysosomes. Lysosomal dysfunction leads to the formation of lysosomal vacuoles.[44] By contrast, AuNC-MHA aggregates are colocalized to autolysosomes and are exocytosed.

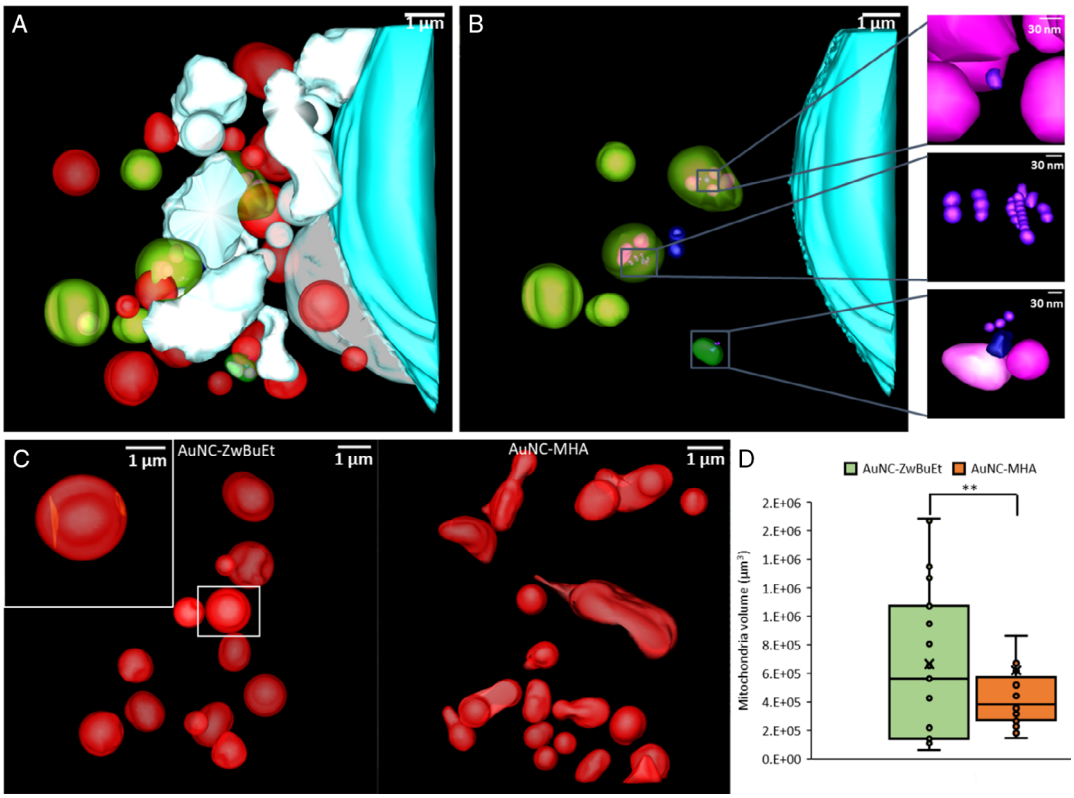

Figure 4. Segmentation of cryo-SXT tomogram of COS-7 fibroblasts exposed to 100 µg Au mL^{-1} AuNC-ZwBuEt for 1 h. A) Color segmentation of organelles of COS-7 fibroblast. B) Color segmentation showing autophagic vesicles and nucleus of COS-7 fibroblast exposed to 100 µg Au mL^{-1} AuNC-ZwBuEt. Inset images show the localization AuNC-ZwBuEt clusters. C) Comparison of mitochondrial morphology of fibroblasts following exposure to AuNC-ZwBuEt or AuNC-MHA. D) Graph comparing the volume distribution of mitochondria in COS-7 fibroblasts following AuNC exposure. Statistical significance is determined by one-way ANOVA and is denoted by $^{**}p < 0.01$, $n = 20$.

cytoprotective response triggered in those fibroblasts exposed to AuNC-ZwBuEt was overwhelmed by an apoptotic response, ultimately leading to the cell's demise. At higher concentrations ($\leq$100 µg mL^{-1} AuNC-ZwBuEt), cell apoptotic response was evidenced by the formation of large intracellular vacuoles, nuclear blebbing, and mitochondrial swelling. Cell necrosis in fibroblasts exposed to AuNC-ZwBuEt was only triggered at higher concentrations of AuNC. Indeed, cell viability assays performed at 24 h, 4 and 7 days postexposure show that at $\geq$100 µg mL^{-1} metabolic activity of the cells is initially reduced compared to nontreated cells, and the cells fail to recover normal proliferative behavior at 4 days posttreatment. The cytoskeletal organization was also impacted as F-actin staining revealed substantial changes to cell shape. Fibroblasts were highly rounded, with radial actin fibers, as opposed to possessing a highly polarized morphology.[42]

As determined in this study, surface chemistry is a crucial factor influencing the biological effect of AuNCs. First, protein coating of the AuNC surface in culture may influence their interactions with the cell membrane and their ultimate uptake and fate within the cell. Nevertheless, it was recently shown that coating the AuNC surface with the ZwBuEt molecule resulted in increased colloidal stability in biological medium with high protein content and an efficient translocation of the coated particle through phospholipid membranes.[23] Indeed, coating particles with zwitterionic or PEGylated molecules has been shown to strongly reduce the formation of a protein corona and increase their half-life in blood.[58] This leads to a significant improvement in their cellular uptake.[10] Furthermore, as AuNC-ZwBuEt aggregates were detected both free within the cytoplasm and the nucleus, energy-independent free translocation and endocytic processes may occur.

The NC surface-ligand density is assumed to be different using a monothiol linker such as MHA as opposed to the bidentate thiol linker used for ZwBuEt. We previously determined the size and the composition of AuNC-MHA and AuNC-ZwBuEt by electrospray mass spectrometry with a molecular weight of 7.5[36] and 13 kDa,[23] respectively. We also performed SAXS measurements achieving shape parameters for AuNC-MHA of a square prism with 0.73 nm sides and a length of 2.27 nm and for AuNC-ZwBuEt, a square prism with sides of 0.79 nm and a length of 2.32 nm.[39] A modified Brust–Schiffrin method was used to synthesize the particle with an excess of ligand to ensure the complete covering of the ligand on the AuNC surface, resulting in a negative surface charge (−21 mV for AuNC-MHA and −10 mV for AuNC-ZwBuEt; Table 1) for both NCs and high colloidal stability. Prior research has shown that thioctic molecules used as a linker led to an approximately fourfold decrease of ligand density compared to short monothiol molecules like

mercaptopropionic acid (1.72 compared to 6.26 ligand per nm^2 for gold nanoparticle with 12 nm diameter).[59] We found a similar trend by X-ray photoelectron spectroscopy (XPS) measurements between AuNC-MHA and AuNC-ZwBuEt[23,36] with ≈4 times less sulfur involved in the binding of ZwBuEt to the gold surface compared to MHA. Thus, it could be that the particles synthesized with MHA ligands have fewer free gold surface atoms, thereby lowering the surface activity in comparison to AuNC-ZwBuEt. However, it is not prudent to only consider the first anchoring to the gold surface as the terminal group of the ligands completely covers the metal core, which will be in contact with the cell surface.

While Au nanoparticles of size 2–8 nm are known to passively interact with lipid membranes regardless of their surface charge,[60–62] recently, we demonstrated the surface-ligand-dependent uptake of AuNC-MHA and AuNC-ZwBuEt and their consequent bactericidal activity to be related to AuNC hydrophobicity and lipophilicity. The antibacterial action of AuNC-MHA (with greater surface hydrophobicity/lipophilicity) toward *Pseudomonas aeruginosa* and *Staphylococcus aureus* bacterial cells was linked to their ability to translocate across the bacterial membrane freely and to bind to subcellular structures such as the bacterial cytoskeleton (and other proteins).[33] On the other hand, AuNC-ZwBuEt were observed to form aggregates at the membrane before being localized within the cell cytoplasm. Using a model membrane (DOPC lipid bilayer produced in a microfluidic device), the authors previously showed that hydrophilic AuNC-ZwBuEt could freely enter the bilayer.[23] Herein, uptake of AuNC-ZwBuEt and AuNC-MHA was assumed to be via endocytosis, although AuNC-ZwBuEt may be able to passively cross lipid bilayers, as evidenced by their localization within the nucleus. Previously, the authors showed that the uptake kinetics of AuNCs protected by ligands of increasing hydrophobicity in human primary glioblastoma and melanoma cell lines highly depended on the ligand and cell line type. Cell uptake was greatest for zwitterionic AuNCs in both investigated cell lines; however, AuNC-ZwBuEt did not induce cytotoxicity at 50 and 100 μg Au mL^{-1}.[23]

Furthermore, we previously showed that AuZwBuEt uptake in dendritic cells was both time and concentration dependent. It was observed that, initially, zwitterionic AuNCs enter the cell and are distributed throughout the cytoplasm, and then, at a later stage, accumulate close to the nucleus. AuNCs were detected in different vesicles, including lysosome/terminal stage endocytic compartments but were not observed inside the nucleus or outside organelles (free within the cytoplasm).[37]

How the AuNCs trigger cell death upon cell entry still requires further investigation. Previous works have identified the role of lysosomal dysfunction that leads to lysosomal membrane permeability and the release of cathepsins into the cytosol, initiating cell apoptosis upon uptake of nanoparticles.[53,63] However, in this work, we have identified impaired mitochondrial function (as determined by cryo-SXT observations of mitochondria morphology, although no AuNC aggregates were found localized to mitochondria)[49] and cell vacuolization due to AuNC exposure at 1 h post-AuNC exposure, as well as a considerable accumulation of AuNC within lysosomes at 24 h and 4 days postexposure. Negatively charged Au nanoparticles that are internalized into cells and accumulate within lysosomes have been found to cause autophagosome accumulation resulting from the blockade of autophagy flux.[64] Additionally, the accumulation of NPs inside lysosomes results in lysosome destabilization, swelling, and inhibition of autophagic flux.[44] The results of this study show that the fibroblasts triggered cell autophagy as a protective response. Autophagosomes ultimately fuse with lysosomes (autophagolysosomes) to degrade engulfed cytosolic contents. It is hypothesized that lysosomal dysfunction occurred, resulting in the observation of the AuNC-ZwBuEt accumulation in lysosomal vacuoles.

4. Conclusion

This work investigated AuNC interactions with COS-7 fibroblasts by tuning cell–particle interactions using surface hydrophobicity/lipophilicity. The two AuNC induced disparate responses in COS-7 cells. In general, AuNC-MHA were not cytotoxic, even at the highest concentrations investigated, and were efficiently transported out of the cell following their uptake in endocytic vesicles. By contrast, AuNC-ZwBuEt were found to adversely impact the health of the fibroblasts. The slight decrease in hydrophobicity of AuNC-ZwBuEt led to efficient translocation of the particles through phospholipid membranes, allowing for their escape from endocytic vesicles. Single AuNC were also found localized to the nucleus after 24 h exposure, and cryo-SXT analysis showed severe cell stress response in the form of swollen mitochondria, nuclear membrane blebbing, and the formation of large vacuoles. The ability of the AuNC to escape endosomes and translocate into the nucleus and other organelles may cause the observed cytotoxicity.[65]

5. Experimental Section

Synthesis of AuNCs: Chemical products were purchased in Sigma-Aldrich (France), and deionized water was used for all synthesis. AuNC stabilized by 6-mercaptohexanoic acid (MHA, $C_6H_{12}O_2S$, $M = 148.2$ g mol^{-1}) was synthesized per our previously described protocols.[33] Briefly, 500 μL of $HAuCl_4 \cdot 3H_2O$ (20 mM) was added to 4.8 mL H_2O followed by 4 mL of the thiolated ligand MHA (5 mM). After 1 min, 500 μL of NaOH (1 M) was added dropwise. After 5 min, 200 μL $NaBH_4$ (20 mM in 0.2 M NaOH) was introduced dropwise under mild stirring. After 4 h, purification of the AuMHA was performed using a 3 kDa cutoff filter column (Amicon). The AuNC-MHA solution was adjusted to pH 7, concentrated to 1 mg Au mL^{-1} in water, and kept refrigerated until required for experiments.

A modified thioctic-zwitterion (ZwButEt, $C_{19}H_{38}N_2O_4S_3$, $M = 455.2$ g mol^{-1}) was synthesized following the protocol described elsewhere.[23] Briefly, $HAuCl_4 \cdot 3H_2O$ (50 mM) was added to an alkaline solution (pH 10) containing the ligand in the presence of the reducing agent $NaBH_4$ (50 mM) and stirred for 15 h. Zwitterion-stabilized Au NCs were synthesized with the molar ratio Au:ZwBuEt:$NaBH_4$ = 1:2:2. Afterward, the solution was filtered 3× with Amicon 3 kDa cutoff filters at 13 600 rpm for 20 min to remove excess free ligand, adjusted to pH 7, concentrated to 1 mg Au mL^{-1} in water, and kept refrigerated until use.

Mammalian Cell Growth Conditions: COS-7 fibroblasts were cultured in Dulbecco's Modified Eagle's medium (DMEM) (Invitrogen) supplemented with 10% fetal bovine serum (FBS) and 1% penicillin–streptomycin at 37 °C and 5% CO_2. The use of the cell line was approved by the Biosafety Project 2014/SBC01. Cells were grown to reach 80% confluency and then trypsinized using 0.25% Trypsin/

EDTA (Invitrogen) and seeded in 96-well-culture plates at 5000 cells cm^{-2} for each independent experiment.

Cell Proliferation: Cell proliferation was determined using the CellTiter 96 Aqueous One Solution Cell Proliferation Assay (Promega, Madison, WI, USA). Tetrazolium was added to the COS-7 cell culture at a 10% ratio of the final volume and incubated for 90 min at 37 °C and 5% CO_2, allowing for the reduction of MTS (3-(4,5-dimethylthiazol-2-yl)-5-(3-carboxymethoxyphenyl)-2-(4-sulfophenyl)-2H-tetrazolium) to formazan, resulting in the formation of a colored precipitate (purple). The absorbance was recorded at a wavelength of 490 nm using a FLUOstar Omega microplate reader (BMG LABTECH, Thermo Fisher Scientific, Waltham, MA, USA).

Fluorescence Microscopy: COS-7 fibroblast cells were incubated with AuNCs for 24 h. Afterward, the samples were washed 3× in warm 10 mM PBS (pH of 7.4) to remove unattached AuNC and transferred to particle-free media and incubated for a further 1, 4, or 7 days. Then the samples were fixed with 4% paraformaldehyde for 15 min, permeabilized in 0.1% Triton X for 5 min, and then blocked with 1% bovine serum albumin (BSA) for 60 min. Image-IT FX Signal Enhancer (Invitrogen, Carlsbad, CA, USA) was also used during the fixation stage to enhance the subsequent fluorescent signals. Actin filaments were visualized by staining the cells with Alexa Fluor 488 conjugated phalloidin (Invitrogen). Cell nuclei were labeled using TO-PRO3 (Invitrogen). Samples were then imaged using a Fluoview FV3000 microscope (Olympus, Tokyo, Japan) at 60× magnification.

TEM: TEM was used to view cross sections of COS-7 fibroblasts incubated with AuNCs. COS-7 fibroblasts were exposed to 100 μg mL^{-1} AuNCs for 24 h. Following the incubation period, the cells were washed to remove nonadherent particles in PBS and then incubated in particle-free media for a further 1-, 4-, or 7 days post-AuNC exposure. The cells were then fixed for TEM preparation as previously described.[39] Briefly, after incubation, cell suspensions were washed to remove any nanoparticles that had not interacted with the cells. The pellets were then fixed using 4% paraformaldehyde in PBS for 15 min and then washed twice in PBS. The cells were postfixed with 1% aqueous osmium tetroxide (OsO_4) for 1.5 h. Samples were then washed and dehydrated by passing them through a graded ethanol series (20%, 40%, and 60%) (2 mL) for 20 min each concentration. The cells were retained overnight in 2% uranyl acetate in 70% ethanol. After staining, the cells were fully dehydrated using ethanol at concentrations of 80%, 90%, and 100% for 15 min each. The embedding medium was prepared using Spurr's resin (ProSciTech) and embedded according to the manufacturers' protocol. Each sample was polymerized for 24 h at 4 °C. The final block was trimmed and then cut into ultrathin sections (50 nm thickness) using a Leica EM UC7 Ultramicrotome (Leica Microsystems, Wetzlar, Germany) with a diamond knife (Diatome, Pennsylvania, USA). Sections were placed onto 300 mesh copper grids and examined using a JEM 1010 instrument (JEOL).

STEM–EDS analysis was performed on samples prepared as described above using a TEM Jeol 2100F (FEG, 200 kV) equipped with a high-angle annular dark field detector (HAADF, scanning TEM mode, STEM) and EDS.

Cryo-SXT: Prior to cell seeding, hydrophilization of quantifoil R 2/2 holey carbon-film Au microscopy grids (Au-G200F1) was achieved by exposure to 1 min O_2 plasma. 2×10^4 COS-7 fibroblasts were seeded onto each grid in a 96-well-plate (Corning) and incubated for 24 h prior to exposure to AuNC. After 1 h of exposure to 100 μg Au mL^{-1} AuNC, Au grids with adhered cells were washed gently with warm PBS and stained for 5 min with Mitotracker (Thermofisher Scientific).

Immediately before plunge-freezing (Leica, EM, GP), 2 μL of 100 nm diameter Au fiducial markers were added to the grids for angular projections alignment prior to tomogram reconstruction. The grids were then blotted from the rear using Whatman filter paper no. 4 to remove the excess medium. The cell distribution and the ice thickness were examined using a cryostage (CMS196 Linkam Scientific Instruments, Epsom, UK)-equipped fluorescence microscope (Zeiss Axio Scope). Grids were transferred to cryo-boxes and stored in liquid nitrogen.

The grids were imaged using the Mistral (ALBA-Light Source) beamline at the ALBA synchrotron (Barcelona, Spain) under cryogenic conditions.[66] Tomography was performed over a tilt range of ± 65° with a step size of 1° at 2.43 nm wavelength (photon energy $E = 520$ eV). Image collection was performed using a 25 nm Fresnel zone plate lens and an image pixel size of 10 nm. Approximately 131 images were acquired for each tilt series with exposure times varying from 1 to 2 s. Tilt series were aligned and reconstructed using IMOD software and segmentation was done with Microscopy Image Browser ver 2.70.

Statistical Analysis: Data are expressed as the mean ± 1 standard deviation (SD) of at least three independent replicates (n). Statistical comparisons were made between data using a one-way ANOVA followed by Tukey's HSD post hoc test where $p \leq 0.05$ denoted a statistically significant difference. Statistical analysis was carried out in IBM SPSS software.

Supporting Information

Supporting Information is available from the Wiley Online Library or from the author.

Acknowledgements

The authors acknowledge the assistance of the RMIT microscopy and microanalysis facility (RMMF). The author Elena P. Ivanova was added as a corresponding author on April 6, 2023 after initial publication online.

Conflict of Interest

The authors declare no conflict of interest.

Data Availability Statement

The data that support the findings of this study are available in the supplementary material of this article.

Keywords

gold nanoclusters, metal nanoclusters, nanotoxicity

Received: July 21, 2022
Revised: December 7, 2022
Published online: February 5, 2023

[1] L. V. Nair, R. V. Nair, S. J. Shenoy, A. Thekkuveettil, R. S. Jayasree, *J. Mater. Chem. B* **2017**, *5*, 42.
[2] L. Shang, G. U. Nienhaus, *Biophys. Rev.* **2012**, *4*, 4.
[3] E. Porret, X. Le Guével, J.-L. Coll, *J. Mater. Chem. B* **2020**, *8*, 11.
[4] Y. Zheng, J. Wu, H. Jiang, X. Wang, *Coord. Chem. Rev.* **2021**, *431*, 213689.
[5] L.-C. Cheng, X. Jiang, J. Wang, C. Chen, R.-S. Liu, *Nanoscale* **2013**, *5*, 9.
[6] A. Cifuentes-Rius, V. G. Deepagan, J. Xie, N. H. Voelcker, *ACS Appl. Mater. Interfaces* **2021**, *13*, 42.
[7] M. F. Matus, H. Häkkinen, *Small* **2021**, *17*, 27.
[8] C. N. Loynachan, A. P. Soleimany, J. S. Dudani, Y. Lin, A. Najer, A. Bekdemir, Q. Chen, S. N. Bhatia, M. M. Stevens, *Nat. Nanotechnol.* **2019**, *14*, 9.
[9] C. Colombé, X. Le Guével, A. Martin-Serrano, M. Henry, E. Porret, C. Comby-Zerbino, R. Antoine, I. Atallah, B. Busser, J.-L. Coll, C. A. Righini, L. Sancey, *Nanomed. Nanotechnol. Biol. Med.* **2019**, *20*, 102011.
[10] X. Le Guével, M. Henry, V. Motto-Ros, E. Longo, M. I. Montañez, F. Pelascini, O. de La Rochefoucauld, P. Zeitoun, J.-L. Coll, V. Josserand, L. Sancey, *Nanoscale* **2018**, *10*, 39.

[11] Y. Chen, D. M. Montana, H. Wei, J. M. Cordero, M. Schneider, X. Le Guével, O. Chen, O. T. Bruns, M. G. Bawendi, *Nano Lett.* **2017**, *17*, 10.
[12] Z. Yu, B. Musnier, K. D. Wegner, M. Henry, B. Chovelon, A. Desroches-Castan, A. Fertin, U. Resch-Genger, S. Bailly, J.-L. Coll, Y. Usson, V. Josserand, X. Le Guével, *ACS Nano* **2020**, *14*, 4.
[13] S. Tang, C. Peng, J. Xu, B. Du, Q. Wang, R. D. Vinluan, M. Yu, M. J. Kim, J. Zheng, *Angew. Chem., Int. Ed.* **2016**, *55*, 52.
[14] D. F. Moyano, K. Saha, G. Prakash, B. Yan, H. Kong, M. Yazdani, V. M. Rotello, *ACS Nano* **2014**, *8*, 7.
[15] Y. Genji Srinivasulu, Q. Yao, N. Goswami, J. Xie, *Mater. Horiz.* **2020**, *7*, 10.
[16] B. Du, X. Jiang, A. Das, Q. Zhou, M. Yu, R. Jin, J. Zheng, *Nat. Nanotechnol.* **2017**, *12*, 11.
[17] K. L. Aillon, Y. Xie, N. El-Gendy, C. J. Berkland, M. L. Forrest, *Adv. Drug Del. Rev.* **2009**, *61*, 6.
[18] H. S. Choi, W. Liu, P. Misra, E. Tanaka, J. P. Zimmer, B. Itty Ipe, M. G. Bawendi, J. V. Frangioni, *Nat. Biotechnol.* **2007**, *25*, 10.
[19] C. Peng, Y. Huang, J. Zheng, *J. Controlled Release* **2020**, *322*, 64.
[20] X.-D. Zhang, Z. Luo, J. Chen, H. Wang, S.-S. Song, X. Shen, W. Long, Y.-M. Sun, S. Fan, K. Zheng, D. T. Leong, J. Xie, *Small* **2015**, *11*, 14.
[21] Z. Liu, Z. Wu, Q. Yao, Y. Cao, O. J. H. Chai, J. Xie, *Nano Today* **2021**, *36*, 101053.
[22] B. D. Chithrani, A. A. Ghazani, W. C. W. Chan, *Nano Lett.* **2006**, *6*, 4.
[23] E. Porret, L. Sancey, A. Martín-Serrano, M. I. Montañez, R. Seeman, A. Yahia-Ammar, H. Okuno, F. Gomez, A. Ariza, N. Hildebrandt, J.-B. Fleury, J.-L. Coll, X. Le Guével, *Chem. Mater.* **2017**, *29*, 17.
[24] C. Y. Tay, Y. Yu, M. I. Setyawati, J. Xie, D. T. Leong, *Nano Res.* **2014**, *7*, 6.
[25] C. Carnovale, G. Bryant, R. Shukla, V. Bansal, *ACS Omega* **2019**, *4*, 242.
[26] Y. Pan, A. Leifert, D. Ruau, S. Neuss, J. Bornemann, G. Schmid, W. Brandau, U. Simon, W. Jahnen-Dechent, *Small* **2009**, *5*, 18.
[27] M. Turner, V. B. Golovko, O. P. H. Vaughan, P. Abdulkin, A. Berenguer-Murcia, M. S. Tikhov, B. F. G. Johnson, R. M. Lambert, *Nature* **2008**, *454*, 7207.
[28] Y. Pan, S. Neuss, A. Leifert, M. Fischler, F. Wen, U. Simon, G. Schmid, W. Brandau, W. Jahnen-Dechent, *Small* **2007**, *3*, 11.
[29] M. Enea, E. Pereira, M. Peixoto de Almeida, A. M. Araújo, M. D. L. Bastos, H. Carmo, *Nanomaterials* **2020**, *10*, 5.
[30] R. Suresh Vs, *J. Toxicol. Risk Assess.* **2021**, *7*, 036.
[31] C. Peng, J. Xu, M. Yu, X. Ning, Y. Huang, B. Du, E. Hernandez, P. Kapur, J. T. Hsieh, J. Zheng, *Angew. Chem., Int. Ed.* **2019**, *58*, 25.
[32] F. Strutz, G. A. Muller, *Nephrol., Dial., Transplant.* **2006**, *21*, 12.
[33] D. P. Linklater, X. Le Guével, G. Bryant, V. A. Baulin, E. Pereiro, P. G. T. Perera, J. V. Wandiyanto, S. Juodkazis, E. P. Ivanova, *ACS Appl. Mater. Interfaces* **2022**, *14*, 32634.
[34] X. Yuan, N. Goswami, W. Chen, Q. Yao, J. Xie, *Chem. Commun.* **2016**, *52*, 30.
[35] M. R. Ivanov, A. J. Haes, *Anal. Chem.* **2012**, *84*, 3.
[36] B. Musnier, K. D. Wegner, C. Comby-Zerbino, V. Trouillet, M. Jourdan, I. Häusler, R. Antoine, J.-L. Coll, U. Resch-Genger, X. Le Guével, *Nanoscale* **2019**, *11*, 25.
[37] T. D. Fernández, J. R. Pearson, M. P. Leal, M. J. Torres, M. Blanca, C. Mayorga, X. Le Guével, *Biomaterials* **2015**, *43*.
[38] Y. Yang, A. Han, R. Li, G. Fang, J. Liu, S. Wang, *Analyst* **2017**, *142*, 23.
[39] D. P. Linklater, X. Le Guével, G. Bryant, V. A. Baulin, E. Pereiro, P. G. T. Perera, J. V. Wandiyanto, S. Juodkazis, E. P. Ivanova, *ACS Appl. Mater. Interfaces* **2022**, *14*, 32634.
[40] B. Dalzon, A. Torres, H. Diemer, S. Ravanel, V. Collin-Faure, K. Pernet-Gallay, P.-H. Jouneau, J. Bourguignon, S. Cianférani, M. Carrière, C. Aude-Garcia, T. Rabilloud, *Environ. Sci.: Nano* **2019**, *6*, 10.
[41] P. Tucci, G. Porta, M. Agostini, D. Dinsdale, I. Iavicoli, K. Cain, A. Finazzi-Agró, G. Melino, A. Willis, *Cell Death Dis.* **2013**, *4*, 3.
[42] W. E. Sinclair, H.-H. Chang, A. Dan, P. J. A. Kenis, C. J. Murphy, D. E. Leckband, *Sci. Rep.* **2020**, *10*, 13320.
[43] T. Mironava, M. Hadjiargyrou, M. Simon, V. Jurukovski, M. H. Rafailovich, *Nanotoxicology* **2010**, *4*, 120.
[44] M. Borkowska, M. Siek, D. V. Kolygina, Y. I. Sobolev, S. Lach, S. Kumar, Y.-K. Cho, K. Kandere-Grzybowska, B. A. Grzybowski, *Nat. Nanotechnol.* **2020**, *15*, 4.
[45] J. Groen, A. Palanca, A. Aires, J. J. Conesa, D. Maestro, S. Rehbein, M. Harkiolaki, A. V. Villar, A. L. Cortajarena, E. Pereiro, *Chem. Sci.* **2021**, *12*, 45.
[46] A. Nakashima, K. Higashisaka, T. Kusabiraki, A. Aoki, A. Ushijima, Y. Ono, S. Tsuda, T. Shima, O. Yoshino, K. Nagano, Y. Yoshioka, Y. Tsutsumi, S. Saito, *Sci. Rep.* **2019**, *9*, 5478.
[47] J. Xu, R. Camfield, S. M. Gorski, *J. Cell Sci.* **2018**, *131*, 15.
[48] E. R. Gran, F. Bertorelle, H. Fakhouri, R. Antoine, M. Perić Bakulić, Ž. Sanader Maršić, V. Bonačić-Koutecký, M. Blain, J. Antel, D. Maysinger, *Nanoscale* **2021**, *13*, 5.
[49] A. Gallud, K. Klöditz, J. Ytterberg, N. Östberg, S. Katayama, T. Skoog, V. Gogvadze, Y.-Z. Chen, D. Xue, S. Moya, J. Ruiz, D. Astruc, R. Zubarev, J. Kere, B. Fadeel, *Sci. Rep.* **2019**, *9*, 4366.
[50] R. Rossignol, R. Gilkerson, R. Aggeler, K. Yamagata, S. J. Remington, R. A. Capaldi, *Cancer Res.* **2004**, *64*, 3.
[51] T. Farmer, N. Naslavsky, S. Caplan, *Traffic* **2018**, *19*, 8.
[52] J. Cheng, Q. Zhang, S. Fan, A. Zhang, B. Liu, Y. Hong, J. Guo, D. Cui, J. Song, *Nanoscale* **2019**, *11*, 47.
[53] S. T. Stern, P. P. Adiseshaiah, R. M. Crist, *Part. Fibre Toxicol.* **2012**, *9*, 20.
[54] R. Andrade, L. Crisol, R. Prado, M. D. Boyano, J. Arluzea, J. Aréchaga, *Biol. Cell* **2010**, *102*, 25.
[55] Y. Guo, E. Terazzi, R. Seemann, J. B. Fleury, V. A. Baulin, *Sci. Adv.* **2016**, *2*, 11.
[56] N. Gunduz, H. Ceylan, M. O. Guler, A. B. Tekinay, *Sci. Rep.* **2017**, *7*, 40493.
[57] R. Gaspar, *Nat. Nanotechnol.* **2013**, *8*, 2.
[58] K. P. García, K. Zarschler, L. Barbaro, J. A. Barreto, W. O'Malley, L. Spiccia, H. Stephan, B. Graham, *Small* **2014**, *10*, 13.
[59] A. M. Smith, K. A. Johnston, S. E. Crawford, L. E. Marbella, J. E. Millstone, *Analyst* **2017**, *142*, 11.
[60] A. Verma, O. Uzun, Y. Hu, Y. Hu, H.-S. Han, N. Watson, S. Chen, D. J. Irvine, F. Stellacci, *Nat. Mater.* **2008**, *7*, 7.
[61] R. C. Van Lehn, P. U. Atukorale, R. P. Carney, Y.-S. Yang, F. Stellacci, D. J. Irvine, A. Alexander-Katz, *Nano Lett.* **2013**, *13*, 9.
[62] E. Canepa, S. Salassi, F. Simonelli, R. Ferrando, R. Rolandi, C. Lambruschini, F. Canepa, S. Dante, A. Relini, G. Rossi, *Sci. Rep.* **2021**, *11*, 1256.
[63] F. Wang, A. Salvati, P. Boya, *Open Biol.* **2018**, *8*, 4.
[64] X. Ma, Y. Wu, S. Jin, Y. Tian, X. Zhang, Y. Zhao, L. Yu, X.-J. Liang, *ACS Nano* **2011**, *5*, 11.
[65] M. Tsoli, H. Kuhn, W. Brandau, H. Esche, G. Schmid, *Small* **2005**, *1*, 8.
[66] A. Sorrentino, J. Nicolás, R. Valcárcel, F. J. Chichón, M. Rosanes, J. Avila, A. Tkachuk, J. Irwin, S. Ferrer, E. Pereiro, *J. Synchrotron Rad.* **2015**, *22*, 1112.